JGR Planets

RESEARCH ARTICLE
10.1029/2018JE005858

Special Section:
Science Enabled by the Lunar Reconnaissance Orbiter Cornerstone Mission

A New Method for Simulation of Lunar Microwave Brightness Temperatures and Evaluation of Chang'E-2 MRM Data Using Thermal Constraints From Diviner

Guangfei Wei[1,2,3], Xiongyao Li[1,3,4], Hong Gan[2,5], David T. Blewett[6], Catherine D. Neish[7], and Benjamin T. Greenhagen[6]

[1]Center for Lunar and Planetary Sciences, Institute of Geochemistry, Chinese Academy of Sciences, Guiyang, China, [2]State Key Laboratory of Lunar and Planetary Sciences, Macau University of Science and Technology, Macau, China, [3]CAS Center for Excellence in Comparative Planetology, Hefei, China, [4]Key Laboratory of Space Manufacturing Technology, Chinese Academy of Sciences, Beijing, China, [5]Analyzing and Testing Center, Guizhou Institute of Technology, Guiyang, China, [6]Planetary Exploration Group, Johns Hopkins University Applied Physics Laboratory, Laurel, MD, USA, [7]Department of Earth Sciences, Western University, London, Ontario, Canada

Abstract We used the bolometric brightness temperatures (T_{Bol}) derived from the Lunar Reconnaissance Orbiters Diviner Lunar Radiometer (Diviner) as an upper boundary condition in our thermal model. We then calculated temperature profiles at any local time based on our improved thermal model at low to middle latitudes (70° N/S). Based on the temperature profiles, we modeled the midnight brightness temperature at 19.35 (T_{B19}) and 37 GHz (T_{B37}). Comparing to the *Chang'E-1* and *Chang'E-2* (CE-1/2) observations, we found that CE-1 showed a better data quality than that of CE-2, especially for the T_{B37} data. Assuming that the issue with the CE-2 data is caused by heat contamination of the cold-reference antennas, we performed an empirical normalization of the CE-2 microwave radiometer data near midnight following the approach of Hu et al. (2017). The results show that T_B difference (modeled values minus modified T_B) for 19.35 GHz is less than 3.40 K for ~80% of the pixels. At 37 GHz, ~67% of the pixels have T_B difference less than 2.88 K. Additionally, we identified some areas of low microwave temperature in our modified T_B maps. These low-T_B features can be characterized by two types: (1) low T_B spots at fresh craters with high rock abundance and bright rays and (2) high-Ti lunar mare surfaces with a low content of rock fragments. Investigating these low-T_B regions with the modified T_B data can reveal more information about subsurface thermal regime and properties and help us better understand the evolution of regolith on the Moon.

Plain Language Summary We proposed a new method to simulate the microwave brightness temperature of the Moon using surface thermal constraints from Lunar Reconnaissance Orbiter Diviner data. We evaluated the Chang'E-1/2 microwave radiometer data and adjusted the midnight observations to account for its calibration uncertainties. Our results provide better constraints on the thermal regime in the subsurface. Of particular interest is microwave cold regions, the presence of which can be related to thermophysical and compositional properties of the regolith in these locations. The modified Chang'E-2 microwave data can also be applied to study the thermal evolution of the Moon.

Key Points:
- A new method using Diviner data to constraint surface temperature is used in our thermal model
- Microwave brightness temperatures at midnight of middle to low latitudes are modeled from improved thermal model
- High frequencies of Chang'E-2 microwave radiometer data near midnight were modified, and brightness temperature maps are created

Correspondence to:
G. Wei and X. Li,
weiguangfei@mail.gyig.ac.cn;
lixiongyao@vip.skleg.ac.cn

Citation:
Wei, G., Li, X., Gan, H., Blewett, D. T., Neish, C., & Greenhagen, B. T. (2019). A new method for simulation of lunar microwave brightness temperatures and evaluation of Chang'E-2 MRM data using thermal constraints from Diviner. *Journal of Geophysical Research: Planets*, *124*, 1433–1450. https://doi.org/10.1029/2018JE005858

Received 20 OCT 2018
Accepted 12 APR 2019
Accepted article online 22 APR 2019
Published online 30 MAY 2019

Author Contributions
Conceptualization: Hong Gan, David T. Blewett, Catherine D. Neish, Benjamin T. Greenhagen
Data curation: Hong Gan, David T. Blewett
Funding Acquisition: David T. Blewett
Methodology: Hong Gan, David T. Blewett, Catherine D. Neish, Benjamin T. Greenhagen
Validation: Hong Gan, David T. Blewett, Catherine D. Neish, Benjamin T. Greenhagen
Writing - Original Draft: Hong Gan, David T. Blewett
Formal Analysis: Hong Gan, David T. Blewett, Catherine D. Neish, Benjamin T. Greenhagen
Investigation: Hong Gan, David T. Blewett

1. Introduction

The lunar regolith is a product of the Moon's geological evolution, formed through billions of years of impact gardening and space weathering. The thermal environment of the lunar surface is dominated by the thermophysical properties of this unconsolidated regolith, and by studying the temperature of the lunar surface, we can learn about its evolution over time. Several ground-based observations with wavelengths from infrared to radio bands have been used to investigate the surface thermal environment and surface properties of the Moon (e.g., Gary & Keihm, 1978; Jones et al., 1975; Linsky, 1966; Pettit & Nicholson, 1930; Sandor, 1995). Most of these observations suffered from calibration difficulties and coarse spatial resolution. In addition, only the nearside of the Moon could be studied with these ground-based observations. Compared with visible and infrared wavelengths, microwave observations can penetrate to a greater depth,

Resources: , Hong Gan, David T. Blewett
Supervision: David T. Blewett
Visualization: Hong Gan, David T. Blewett
Writing - review & editing: Hong Gan, David T. Blewett

providing complimentary information about the physical and chemical properties of the regolith. These properties include thickness, dielectric permittivity, and composition. Since the 1980s, passive orbital microwave measurements at different frequencies were proposed to investigate global heat flow, estimate average regolith thickness, and evaluate He-3 content on the Moon (e.g., Fa & Jin, 2007a; Keihm, 1984; Keihm & Cutts, 1981; Shkuratov & Bondarenko, 2001). Similar to thermal-infrared techniques, microwave sensors can observe the lunar surface regardless of solar diurnal illumination variations, which is advantageous for measuring the subsurface temperature and for determining regolith thermal properties within permanently shadowed regions at the lunar poles (Chan et al., 2010; Meng et al., 2010; Wei et al., 2016b).

China successfully launched the Chang'E-1 (CE-1) and Chang'E-2 (CE-2) satellites on 24 October 2007 and 1 October 2010, respectively. Over the course of those missions, the Microwave RadioMeter (MRM) onboard both orbiters obtained repeat coverage of global microwave brightness temperature (T_B) at four frequencies (Fang & Fa, 2014; Zheng et al., 2012). Based on observed and modeled T_B, a number of inversion schemes have been developed to investigate lunar regolith thickness (Fa & Jin, 2010; Zhou et al., 2010), He-3 content (Fa & Jin, 2007a), dielectric constant (Gong et al., 2015; Wang et al., 2010), and subsurface temperatures (Gong & Jin, 2012; Wei et al., 2016a). However, these studies assumed a smooth spherical model for calculating lunar surface temperature. That means those simulations of T_B only took into account the effects of latitude, local time, and surface albedo variations in governing the surface temperature. For the nadir-viewing observations of the CE-1/2 MRMs, the terrain's scattering and shading effects on microwave brightness temperature can be ignored. However, the anisotropy of surface temperature caused by partial illumination within the MRM field of view can lead to large uncertainties in T_B (Wang et al., 2010). Meng et al. (2014) improved the surface temperature model by taking the lunar topography into account based on topography data from the CE-1 Laser Altimeter. However, they assumed the global homogeneity of thermal emissivity and albedo—quantities which, on the real Moon, vary depending on latitude, regolith composition, and rock abundance. In order to reduce the influence of topography, Fang and Fa (2014) considered a more realistic lunar surface to simulate surface temperature. However, they neglected the scattering effects of solar and infrared energy between adjacent surface elements and the inhomogeneity of surface emissivity, which could introduce uncertainties into the simulated surface temperature and T_B.

The accurate calculation of lunar surface/subsurface temperatures can make T_B simulation more reliable, because T_B is highly dominated by regolith temperatures. During the lunar daytime, the surface temperature equilibrates with incident solar flux because of the highly insulating nature of the regolith, the Moon's lack of a substantial atmosphere, and the slow rotation of the Moon. Thus, these factors can cause large variations in temperature in the near surface as a result of variations in solar flux and surface heat exchange (Keihm & Cutts, 1981). At low solar incidence angles, for example, surface temperatures are controlled by topographic effects, thermal-scale surface roughness, infrared emissivity, and surface albedo. At higher incidence angles, the topographic and roughness effects become dominant resulting in temperature anisotropy and anisothermality (Williams et al., 2017). Over the course of the lunar night, the surface temperatures monotonically decrease until sunrise due to the heat loss. Additionally, the surface temperature of the Moon represents a fundamental boundary condition that governs the regolith thermal regime and even the behavior of near-surface volatiles within permanently shadowed regions (Paige et al., 2010). Therefore, accurate constraints on surface temperature are crucial for proper simulation of T_B and for retrieving regolith information from microwave observations.

The global, diurnal coverage of MRM T_B data provides valuable information for interpreting the physical properties of the lunar regolith and characterizing its thermal behavior. Recently, validation of the CE-1 and CE-2 MRM data sets has been carried out by Hu et al. (2017). Based on the comparisons of modeled T_B and CE-1/2 observations at the Apollo 15 and 17 landing sites, they found that the CE-1 MRM data set is more accurate than that of CE-2. The uncertainties of the CE-2 data set might be caused by heat contamination received by the MRM cold-reference antennas during the on-orbit calibration (Hu et al., 2017). Those workers proposed a recalibration approach for the two data sets based on the comparison of the CE-1/2 measurements and theoretical calculations of T_B at the Apollo 15 and 17 landing sites. However, the T_B simulation in Hu et al. (2017) was based on a smooth spherical thermal model without considering the effects of topography, surface roughness, emissivity, or albedo. In addition, the two Apollo landing sites included in their T_B comparison might not be representative of other areas of the Moon. Therefore, it is useful to reassess and modify the CE-2 MRM data to more accurately investigate the surface thermal envi-

ronment and physical properties of the lunar regolith at global scales and to consider a method for empirical adjustment of the data to potentially compensate for the contamination of the reference antennas.

The Diviner Lunar Radiometer (Diviner) onboard the *Lunar Reconnaissance Orbiter* (LRO) spacecraft has systematically mapped the lunar surface thermal environment since 2009 (Paige et al., 2010). The thermal emission recorded by Diviner is a function of complicated features within a scene, including small-scale slopes and rocks, as well as the material thermophysical properties (Vasavada et al., 2012). Diviner measurements offer a more accurate source of surface temperatures on the Moon throughout the diurnal cycle compared with theoretical temperature models. Although extensive analysis of surface temperature and regolith thermal properties has been performed based on Diviner data (e.g., Bandfield et al., 2015; Hayne et al., 2017; Paige et al., 2010; Vasavada et al., 2012; Williams et al., 2017), there are few systematic investigations of subsurface temperature as constrained by Diviner measurements (Hayne et al., 2017; Siegler et al., 2015). In this study, we present a new method to improve the accuracy of MRM T_B modeling, based on Diviner data. With the improved T_B simulations enabled by Diviner data, the normalization of the CE-2 MRM data becomes possible. In turn, more detailed information on the lunar regolith can be extracted from the modified MRM observations.

In section 2, we present a brief description of the Diviner data, bolometric brightness temperature, and the CE-1/2 MRM data. Our modeling approach, including the thermal model and simulation of microwave brightness temperature, is introduced in section 3. Section 4 presents the calculated averaged diurnal subsurface temperatures and modeled microwave brightness temperatures at midnight. In section 5, we verify our simulation results by comparing them to the CE-1 MRM data sets. Upon evaluation of the CE-2 MRM data, we perform an empirical adjustment using the model results. We also present geological interpretations of features identified in our modified T_B maps. In section 6, we summarize our work and present the conclusions.

2. Data Sets

2.1. Diviner Data

The LRO was launched on 18 June 2009 and transitioned into a near-circular, 2-hr period mapping orbit with an average altitude ~50 km on 15 September (Williams et al., 2017). LRO left this circular orbit for a low energy 30-km 200-km elliptical orbit on 11 December 2011. The Diviner experiment onboard LRO is a nine-channel radiometer with two spectral channels from 0.35 to 2.8 μm for reflected solar radiation and seven channels for infrared emission, spanning 7.55 to ~400 μm (Paige et al., 2010). Each channel consists of an array of 21 detectors that are nominally nadir-pointing, collecting data in a push-broom configuration (Paige et al., 2010). The footprint at the nominal 50-km observation altitude is ~3.4 km, with a spatial resolution of 320 m by 160 m in the along- and cross-track directions, respectively (Paige et al., 2010). One of the scientific goals for Diviner is to globally map lunar surface temperature and characterize regolith thermal properties over diurnal and seasonal cycles (Hayne et al., 2017; Vasavada et al., 2012; Williams et al., 2017), including the extremely low temperatures within the permanently shadowed regions near the poles (Hayne et al., 2010; Paige et al., 2010).

To date, Diviner has acquired a large quantity of data covering a full range of local times (Hayne et al., 2017; Williams et al., 2017). High-resolution temperature maps generated with this data set provide a global perspective on the surface energy balance of the Moon and reveal the complicated nature of the lunar surface thermal environment (Paige et al., 2010; Williams et al., 2017). Additionally, the diurnal variations of surface temperature characterized by Diviner measurements place strong constraints on the thermal state of the subsurface (Paige et al., 2010). This information can be used to characterize surface properties such as thermal inertia and rock abundance and to determine the locations and temperatures of volatile cold traps in the lunar polar regions (e.g., Bandfield et al., 2011; Hayne et al., 2010; Paige et al., 2010).

Due to the nonlinear nature of Planck radiance with respect to wavelength, the warmer surface temperatures have a proportionally greater effect on infrared brightness temperatures in the shorter-wavelength Diviner channels (Paige et al., 2010). In addition, surface temperatures are highly sensitive to regolith albedo and thermophysical properties and wavelength-dependent emissivity. Therefore, the observed infrared brightness temperatures cannot be directly interpreted in terms of a unique surface temperature. The bolometric brightness temperature (T_{Bol}) is a measure of the spectrally integrated flux of infrared radiation emerging from the surface; this quantity was first derived from Diviner measurements by Paige, Siegler, and Zhang

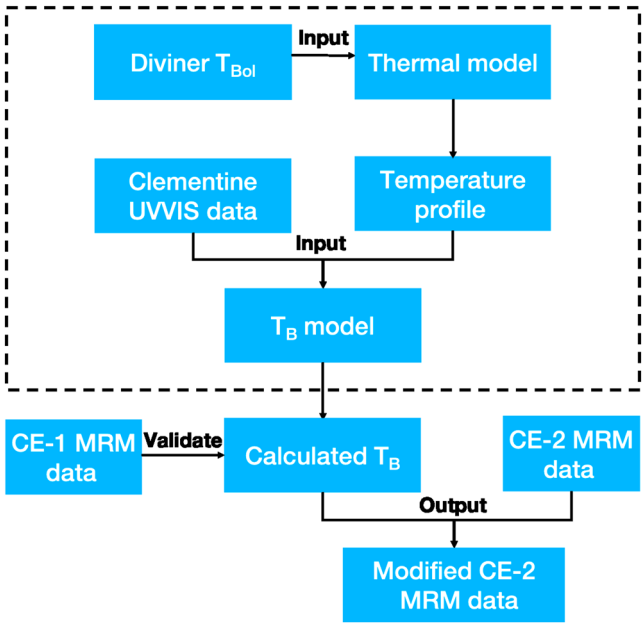

Figure 1. Flowchart of T_B simulation and CE-2 MRM data modification. The dashed box represents the process of T_B simulation at each cell. UVVIS = ultraviolet-visible; MRM = Microwave RadioMeter.

(2010). T_{Bol} is more directly related to the surface thermal balance and can represent the lunar surface temperature.

Recently, Williams et al. (2017) compiled Diviner observations from 5 July 2009 to 1 April 2015 (over 25,000 orbits) into bins of 0.5 latitude and longitude and 0.25 hr of local time to characterize the diurnal variation of the surface thermal conditions. This data set is of high quality and can serve as a constraint for thermal modeling. These data products were generated by the Diviner science team and archived as Global Cumulative Products which are now available at the Planetary Data System Geosciences Node. Notably, T_{Bol} includes the effects of surface roughness, rock abundance, albedo, infrared emission, and multiple light scattering in the footprints of Diviner. Therefore, the diurnal variation of T_{Bol} on the Moon provides us with high-quality surface temperature constraints for our microwave T_B simulations.

2.2. CE-1/2 MRM Data

The MRM onboard CE-2 is the second radiometer to fly on a lunar orbiter after its predecessor on CE-1 (Wang et al., 2010). The scientific objectives of the MRMs onboard both missions were to obtain global subsurface T_B of the Moon, retrieve lunar regolith information, and evaluate the distribution of He-3 in the surface. The MRMs observed microwave emissions from the surface with four nadir-viewing antennas operating at 3, 7.8, 19.35, and 37 GHz (10-, 3.84-, 1.55-, and 0.81-cm wavelengths). CE-1 mapped the Moon 8 times during its ~16 months of observation, while CE-2 mapped the Moon ~15 times during its ~8-month mission. As CE-2 had a lower orbital altitude than did CE-1 (~100 vs. ~200 km), the spatial resolution of CE-2 observations are improved by a factor of 2 compared with CE-1. The CE-2 MRM spatial resolution is ~25 km at 3 GHz and 15 km in the other channels. The radiometric resolutions at the four channels are 0.16, 0.16, 0.12, and 0.14 K, which are better than the CE-1s 0.5 K (Wang et al., 2010). More details about the major technical specifications and preprocessing of MRM data can be found in Zheng et al. (2012).

Calibrations on both missions were done using measurements of a high-temperature onboard source and data from cold space-looking reference horns (Wang, Li, Zhang, Jiang, Xu, et al., 2010; Wang, Li, Zhang, Jiang, Zhao, et al., 2010). The final level 2C MRM data products are archived in the format of the Planetary Data System and were used in our study. To obtain the local time from the metadata for each observation cell, we employed the method of Zheng et al. (2012) which is based on the solar incidence and azimuth angles and latitude. It is worthwhile to note that most of the CE-1 observations are concentrated in the local times of 10:00–14:00 and 22:00–02:00, while the CE-2's observations more uniformly cover the entire lunar day.

Figure 1 shows the flowchart of the work to simulate subsurface T_B by using surface T_{Bol} data. The Diviner T_{Bol} data are used as an input upper boundary condition in our thermal model. We model subsurface T_B at each cell (0.5° × 0.5°) based on the derived temperature profiles and ilmenite content retrieved from *Clementine* ultraviolet-visible data. Because of the higher calibration accuracy of the CE-1 MRM data (Hu et al., 2017), we apply this data set to validate our modeled T_B. Finally, we compare the simulated subsurface T_B with the CE-2 observations in the range of 70° N/S latitude and modify the CE-2 MRM data.

3. Simulation Approach

3.1. Thermal Model

To accurately simulate T_B based on an assumed regolith stratigraphy, it is important to establish a physical thermal profile model of the Moon's subsurface. In the uppermost layers, regolith samples from Apollo missions are observed to be composed of finer-grained, highly porous material characterized by low bulk density and thermal conductivity. With increasing depth, the density and conductivity increase dramatically, and the influence of larger rock fragments becomes dominant (Carrier et al., 1973; Keihm & Langseth, 1973). This would make the subsurface more conductive to the absorbed solar energy and internal heat flow.

Here we treat each cell as a discrete vertical column and neglect the latent heat. Therefore, the time- and depth-dependent subsurface temperatures can be calculated by solving the one-dimensional heat diffusion equation (e.g., Hayne et al., 2017; Vasavada et al., 1999)

$$\rho(z)C(z,T)\frac{\partial T(t,z)}{\partial t} = \frac{\partial}{\partial z}\left[K(z,T)\frac{\partial T(t,z)}{\partial z}\right], \tag{1}$$

where $T(t,z)$ is subsurface temperature at a given depth, z (cm), and local time, t (s). ρ is regolith density (kg/m^3), C is specific heat (J·kg^{-1}·K^{-1}), and K is thermal conductivity (W·m^{-1}·K^{-1}). The density profile is characterized as a function of depth by fitting the equatorial infrared brightness temperatures from Diviner observations (Vasavada et al., 2012)

$$\rho(z) = \rho_d - (\rho_d - \rho_s)e^{-z/H}, \tag{2}$$

where ρ_s is the density at the surface, and it is updated to 1,100 kg/m^3 in the work of Hayne et al. (2017), and ρ_d = 1,800 kg/m^3 is the density at depths $z \ggg H$. The parameters $C(T)$ and $K(T)$, which are highly dependent upon temperature, have been discussed in detail in previous work such as Hayne et al. (2017), Ledlow et al. (1992), and Vasavada et al. (2012, 1999). Here we follow the method of Hayne et al. (2017) to calculate the density, specific heat, and thermal conductivity.

Now that all the parameters have been defined, we need an upper and a lower boundary conditions to solve equation (1). For the upper boundary condition, we consider the temperature of the lunar surface. At the surface of the Moon, daytime temperatures are primarily controlled by surface energy balance through albedo, roughness, and emissivity, whereas nighttime temperatures are controlled by the thermophysical properties of materials (Hayne et al., 2017). Lunar regolith is highly insulating due to its low density and thermal conductivity (Keihm & Langseth, 1973), and therefore, internal heat flux into the surface during the day is small compared to the incident solar flux (Vasavada et al., 2012). The absorbed heat and conduction at the surface are balanced against infrared emission to space which can be expressed as (Hu et al., 2017)

$$K_s\frac{\partial T}{\partial z}\bigg|_{z=0} = \varepsilon_{IR}\sigma_B T_s^4 - (1-A)\left[I(t)+E(t)\right], \tag{3}$$

where ε_{IR} is infrared emissivity, A is surface albedo, σ_B is Stefan-Boltzmann constant. $I(t)$ and $E(t)$ are solar irradiance and earthshine, respectively. The lower boundary condition at the depth of z_d is dominated by geothermal heat flux Q, and when thermal equilibrium is achieved it can be written as

$$K_d\frac{\partial T}{\partial z}\bigg|_{z=z_d} = -Q, \tag{4}$$

where $\frac{\partial T}{\partial z}\Big|_{z=z_d}$ and K_d are the temperature gradient and heat conductivity evaluated at $z = z_d$, which is selected to be sufficiently deep within the subsurface. Based on the reanalysis of long-term measurements of subsurface temperature at Apollo 15 and 17 landing sites, Langseth et al. (1976) revised the heat flow to 0.021 and 0.014 W/m^2, respectively. They also estimated an average global heat flow of 0.018 W/m^2 from

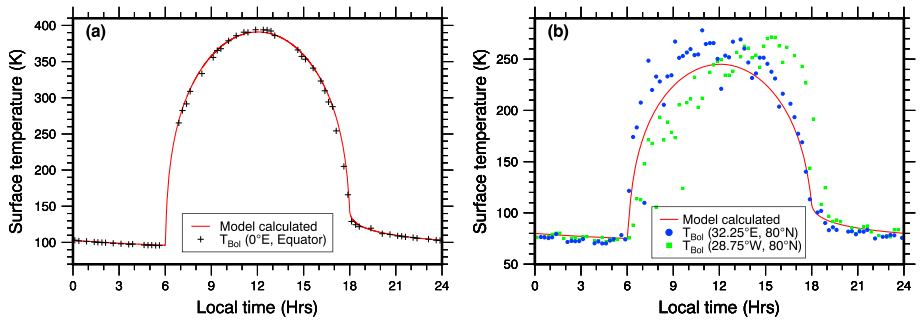

Figure 2. Comparison of surface temperatures calculated from a thermal model to T_{Bol} at (a) the equator and (b) high latitude. The surface albedo, A, used in the calculations was 0.07 in (a) and 0.16 in (b) based on Vasavada et al. (2012). Both calculations used infrared emissivity $\epsilon_{IR} = 0.98$, Earthshine $E(t) = 0.095$ W/m^2, and a mean solar constant of 1,366 W/m^2 (Huang, 2008).

radioactive element abundance and inferred crustal thickness. The large heat flow differences at the two landing sites make us hesitant to assign the Q values for each bin within low to middle latitudes of the Moon. Instead, we employed Langseth et al.'s (1976) mean value in the lower boundary condition for our thermal model.

Generally, equation (3) is considered the key upper boundary condition needed to solve the time-dependent surface temperature in equation (1). However, the thermal environment of the lunar surface is very complicated in the daytime due to shadowing effects and thermal-scale surface roughness caused by the presence of microscale craters and rock fragments (Bandfield et al., 2015). These result in multiple light scattering and anisotropic emission, producing substantial departures from an ideal spherical model. As an example, Figure 2 shows the diurnal variation of surface temperatures that have been calculated from equation (3) and from T_{Bol} data. At low latitudes (Figure 2a), the calculated model temperatures agree well with the Diviner temperatures. However, at high latitudes (80° N, Figure 2b), there are major discrepancies through the day. The irregular nature of the discrepancies in the daytime data suggests that local topography is affecting the measured temperatures within the bin. Thus, model calculated surface temperatures could lead to large uncertainties in the subsurface temperatures, degrading the accuracy of T_B simulations, especially for high latitudes. Note that an improved thermal model considering topographic relief at high latitudes, for example, a 3-dimensional ray tracing model (e.g., Paige et al., 2010) to account for the incident and scattered solar radiation and emitted and scattered thermal radiation, could provide more constraints for surface temperature simulation. Here we focus on the 1-dimensional thermal model that benefits from improved from surface thermal constraints by incorporating surface T_{Bol} data.

As a result, in this work we use the diurnal variation of T_{Bol} as an upper boundary condition instead of equation (3) to solve equation (1). In this way, we aim to derive more realistic subsurface temperatures for our T_B simulation at low to middle latitudes (within 70° of the equator). Additionally, we employ the widely used Crank-Nicholson (Crank & Nicolson, 1947) scheme to solve equation (1) because of its unconditionally stable solution.

3.2. Simulation of Microwave Brightness Temperature

The lunar regolith has been shaped by impact gardening and space weathering for billions of years. The composition and bulk density vary with depth and thus have effects on the propagation of electromagnetic waves via changes in absorption, emission, and volume scattering. Thus, the vertical structure of the regolith plays a major role in the simulation of microwave brightness temperature, T_B. In addition, stratification of the regolith influences not only radiative transfer in the subsurface and reflection at boundaries but also the temperature profile, density, and dielectric properties (Feng et al., 2010). Therefore, brightness temperatures are in turn diagnostic of regolith microwave emissivity and the subsurface thermal regime.

To study the microwave emission from the lunar surface, it is important to understand the role of the regolith permittivity. The lunar regolith is known to be dielectric in nature and generally lacking any strong magnetic component. Thus, the complex permittivity, ϵ , is the main factor affecting radiative transfer in the regolith.

The microwave emissivity (e) of the surface can be simplified to (Pabari, 2016)

$$e = 1 - r = 1 - \left| \frac{1 - \sqrt{\varepsilon}}{1 + \sqrt{\varepsilon}} \right|^2, \tag{5}$$

where r is the Fresnel power reflection coefficient for normal incidence. Since the regolith can be considered to consist of discrete layers (Montopoli et al., 2011) of smaller size, T_B can be simulated for MRM's nadir observing conditions as

$$T_B(\nu, t) = e \cdot \int_0^\infty \kappa_\alpha(\nu, z) T(t, z) e^{-\int_0^z \kappa_\alpha(\nu, z')\mathrm{d}z'} \mathrm{d}z, \tag{6}$$

where $\kappa_\alpha(\nu, z)$ is the depth-dependent power absorption coefficient, $\kappa_\alpha(\nu, z) = (2\pi\nu/c)\sqrt{\varepsilon'(z)}\tan\delta$, ν is the frequency, $\tan\delta = \varepsilon''(z)/\varepsilon'(z)$ is the loss tangent of the material, and $\varepsilon^{'}(z)$ and $\varepsilon^{''}(z)$ are the real and imaginary parts of the effective dielectric constant, respectively.

Laboratory measurements of Apollo regolith samples show that within the temperature variation range of the Moon, the real part of the dielectric constant depends primarily on bulk density, and the loss tangent is a strong function of bulk density, chemical composition, and frequency (Carrier et al., 1991). The real part of the dielectric constant for lunar materials is approximated with $\varepsilon^{'}(z) = 1.919^{\rho(z)}$ for all Apollo samples. After reanalyzing measured dielectric properties of Apollo regolith samples, Fa and Wieczorek (2012) found that the dielectric properties of the regolith might be expected to depend primarily upon TiO_2 content and only secondarily on FeO content. Fa and Wieczorek (2012) obtained the best-fit equation for loss tangent when the data are normalized to a constant density of $\rho = 1.7$ g/cm^3, $\tan\delta = 10^{-2.395+0.064\mathrm{TiO_2}}$. The content of TiO_2 with a resolution of 0.5° per pixel has been derived from *Clementine* ultraviolet-visible data based on the revised algorithm of Gillis et al. (2003); this algorithm applies to both mare and highland surfaces. Considering the effects of regolith porosity, the profile of effective permittivity of the regolith can be calculated following the method of Fa and Wieczorek (2012).

Apollo in situ measurements showed that most of the lunar surface consists of a fine-grained regolith layer that covers the underlying, highly fractured basement materials (i.e., megaregolith). The average thickness of the fine-grained regolith layer is 4–5 m for the maria and 10–15 m for the highlands (Fa & Jin, 2010; Montopoli et al., 2011; Shkuratov & Bondarenko, 2001). The penetration depths of 19.35- and 37-GHz microwaves are no more than 1 m on the Moon (Fang & Fa, 2014; Wang et al., 2010), which is smaller than the typical thickness of the regolith. Therefore, for thermal emission modeling at high MRM frequencies, the lunar regolith can be modeled as a half-space inhomogeneous medium. In this work, the temperature profiles from the surface to 2-m depth have been calculated from our thermal model using the Diviner data as a constraint. Then we simulated global brightness temperatures at 19.35 and 37 GHz based on the calculated temperature profiles.

4. Simulation Results

4.1. Subsurface Temperature

Once we input the T_{Bol} as the upper boundary condition at each cell for our thermal model, we ran the model to calculate subsurface temperatures. However, we find that the time interval of the available T_{Bol} data in some cells varies by 0.25/0.5/1.0 hr, and it is incompatible with the fixed time step in our thermal model. Hence, we interpolate the T_{Bol} data by a piecewise spline method at each cell to generate a uniformly distributed data set with a time step of 0.1 hr. We cautiously use this approach to avoid any additional "noise" that changes the characteristics of T_{Bol} diurnal variations. As a result, the interpolated T_{Bol} data sets move our work forward in two ways: (1) The fixed time step of interpolated data at each cell makes running our thermal model possible. (2) We can derive 240 temperature profiles at different local times at each cell during a lunar day. Thus, we can simulate T_B at greater temporal resolution (compared to 96 temperature profiles at a time step of 0.25 hr) which provides more modeled T_B selections to match the local time of CE-2 observations. As an example shown in Figure 3, the time- and depth-dependent temperatures near the center of the nearside (0° N, 0° E) of the Moon have been calculated using the aforementioned method. It is worth noting

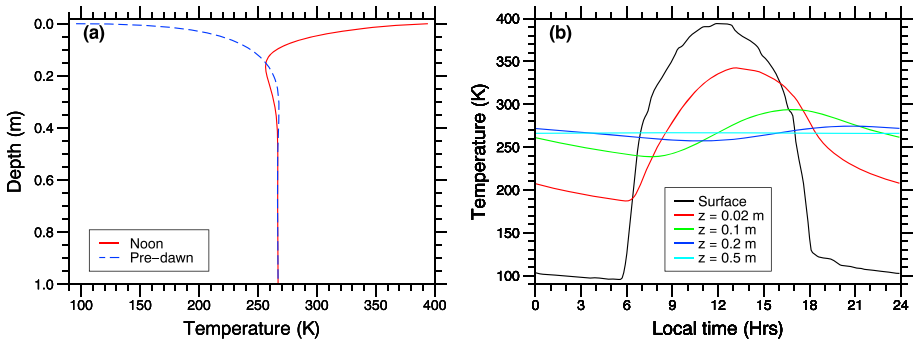

Figure 3. Calculated subsurface temperature near the center of the nearside (0° N, 0° E) of the Moon using our improved thermal model. (a) The depth-dependent temperatures at noon (red line) and predawn (blue line) are shown. (b) Diurnal variation of subsurface temperatures. Note that the surface temperature shown here is plotted based on T_{Bol} values.

that the diurnal variation of subsurface temperatures has also been well constrained by Diviner observations in our thermal model.

Based on the derived temperature profiles in each cell, we can calculate the averaged diurnal subsurface temperature at a certain depth. Figure 4 shows as an example the averaged diurnal temperature at a the depth of 1 m. The temperature decreases from the equator to high latitudes as a result of decreasing solar irradiance. It also reveals that the subsurface temperature is controlled by topographic relief, especially at high latitudes. Furthermore, Figure 4 shows that the subsurface temperatures of the maria are higher than those of the highlands, which can be attributed to differences in surface albedo, emissivity, and/or the thermophysical properties of mare versus highland regolith. Note that the subsurface temperatures at this depth are relatively stable over the course of a diurnal cycle. However, in the shallow depths ($z < 0.2$ m), the subsurface temperature varies substantially in a lunation. It can be inferred that the highest-frequency MRM channel (37 GHz) is more sensitive to the variations of surface temperature due to its shallow penetration depth compared with the other, lower-frequency, MRM channels.

4.2. Simulated Microwave Brightness Temperature

In this section, we present the modeled T_B at 19.35 (T_{B19}) and 37 GHz (T_{B37}) at the low to middle latitudes of the Moon based on calculated temperature profiles. Although the T_{Bol} data sets provide sufficient and accurate surface thermal constraints for our model, the topographic relief still plays an important part in subsurface T_B simulation of daytime T_B. To simulate daytime T_B most accurately, additional factors such as 3-D topographic shielding, light scattering, and rock concentration should be taken into account. Here we focus only on the midnight T_B simulation to evaluate the CE-2 MRM data.

Figure 5 shows the modeled midnight T_{B19} and T_{B37} for latitudes between 70° N and 70° S. Both T_{B19} and T_{B37} decrease with increasing latitude. This is caused by the variation of solar-driven temperature across the Moon, similar to the derived subsurface temperature shown in Figure 4. The maximum T_{B19} is 237.2 K, which is larger than 235.8 K at T_{B37}, and the minimum T_{B19} is 126.6 K, which is about 4.3 K greater than that of T_{B37}. For mare regions, T_{B19} is also larger than that of T_{B37} due to the greater penetration depth of 19.35 GHz. Notably, some geologic features such as Mare Orientale (19.4° S, 92.8° W) and Mare Moscoviense

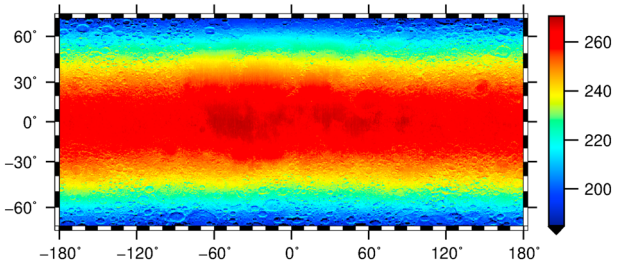

Figure 4. The distribution of calculated diurnal mean temperatures at 1-m depth based on the surface thermal constraint from T_{Bol}.

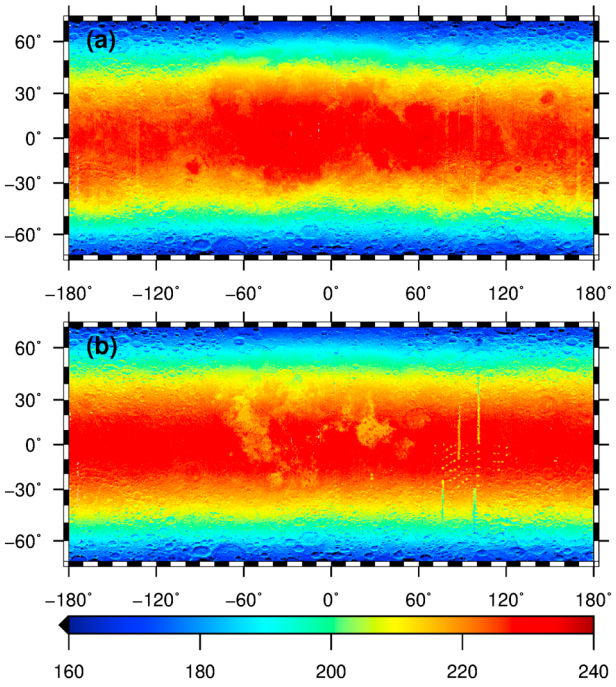

Figure 5. Distribution of model calculated (a) T_{B19} and (b) T_{B37} at midnight on the Moon (within 70° N/S).

(27.3° N,147.9° E) are prominent in the T_{B19} map but are less visible in the T_{B37} map. This indicates that the subsurface thermal regime related to the regolith components, fragments, and compactness behaves differently at different depths. Furthermore, the topography effect plays an important role in the modeled T_{B19} and T_{B37}, especially at high latitudes. For example, at latitudes greater than 60° N/S, the crater walls that face the equator exhibit higher T_B values than those that face the poles.

CE-1 midnight maps of T_{B19} and T_{B37} (Zheng et al., 2012) show that the surface is dotted by many spots that stand out from the surroundings with low T_B values. These cold areas generally correspond to relatively young, rayed impact craters, which were formed in the Copernican period (Zheng et al., 2012). The low-T_{B19}/T_{B37} spots do not appear in our simulation result because variables related to local geology such as rock abundance and regolith maturity have not been taken into account in our thermal model. It is worth-

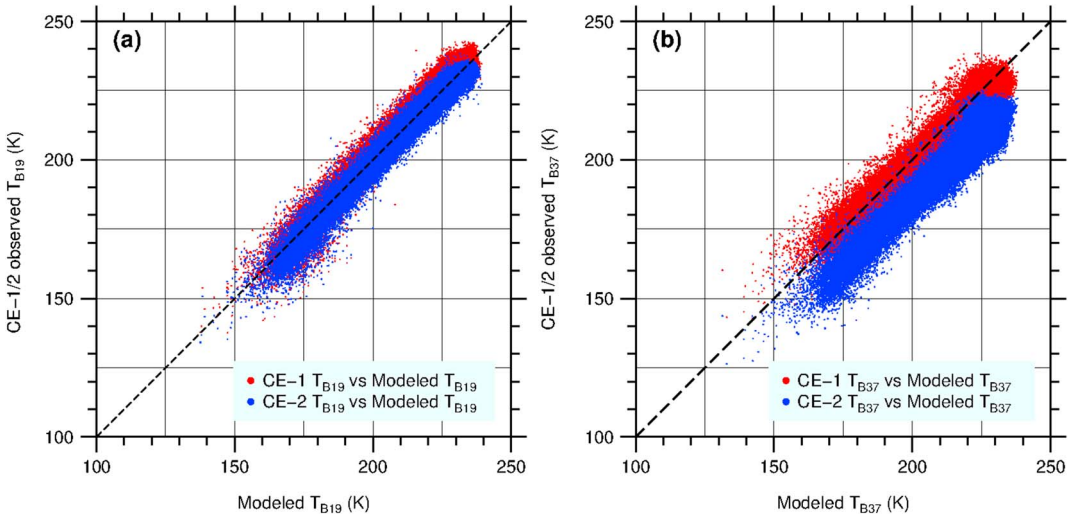

Figure 6. T_B comparisons between CE-1 (red) and CE-2 (blue) observations and our simulation results at (a) 19.35 and (b) 37 GHz near midnight. The dashed lines are 1:1 lines. Each data point corresponds to the same local time of CE-1 and CE-2 observations and modeled T_B.

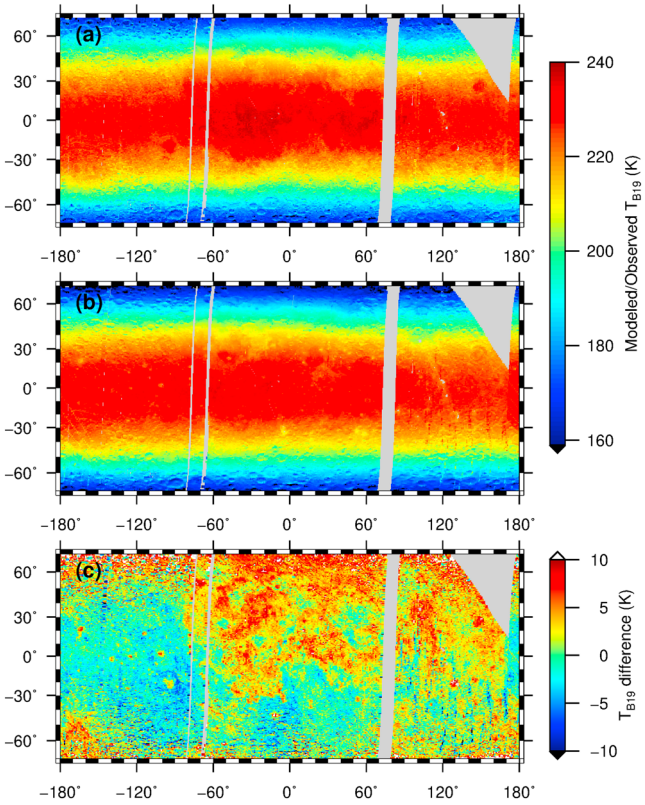

Figure 7. Comparison of T_{B19} near midnight. (a) Model calculated T_{B19}. (b) CE-2 T_{B19} observations. (c) T_{B19} differences between model calculated and CE-2 observations near midnight within 70° N/S latitudes. The gray gaps denote the lack of coverage of CE-2 Microwave RadioMeter data within the time range 23:00–01:00.

while to note that some midnight cold areas such as Mare Tranquillitatis and parts of Oceanus Procellarum have brightness temperatures in Figure 5b at 37 GHz that are lower than the surrounding areas. In particular, basalts with higher ilmenite ($FeTiO_3$) content, such as those in Mare Tranquillitatis and parts of Oceanus Procellarum, have higher loss tangents. The high loss tangent tends to suppress microwave emissions more at higher frequency during nighttime, leading to lower T_B values (Blewett et al., 2018; Zheng et al., 2019).

5. Validation and Evaluation of CE-2 MRM Data

5.1. Validation of Simulation and Evaluation of CE-2 MRMs Nighttime Data

As mentioned above, although the spatial resolution of the CE-1 MRM map (30 km for 19.35 and 37 GHz) is coarser than that of CE-2 MRM (15 km for 19.35 and 37 GHz) and our model simulation (which is equal to the spatial resolution of T_{Bol}, 0.5° bins), theoretical simulations show that there is a less than 2-K T_B difference caused by varying spatial resolution from 35 to 1 km (Hu et al., 2016). Statistically, to validate our simulation results, we need to compare the modeled T_{B19} and T_{B37} to CE-1 observations at the same local time and coverage. In addition, to assess CE-2 observations, we also need to select the CE-2 MRM data at the same local time and resolution with our model simulation. Thus, both the CE-1 and CE-2 MRM data are selected using the following rules: (1) The two data sets are binned into 0.5° × 0.5° cells at midlatitudes. Since the footprint of CE-1's MRM is larger than the cell size, any data points where the center of the footprint is located in the cell are accepted. The footprint of CE-2 MRM is approximately the same size as the cell and so can be compared with the model simulation. (2) For repeated coverage of CE-2 observations at each cell, we selected the data point where the local time is the nearest to midnight within the local time from 23:00 to 01:00. (3) We select the CE-1 data point whose local time is the same as CE-2's at the same cell within 70° N/S latitudes.

The comparison between CE-1 observations and model calculated T_B within 70° N/S is shown in Figure 6 (red points). Both model calculated T_{B19} and T_{B37} show a good agreement with the CE-1 observations. Additionally, Figure 6a shows that both CE-1 and CE-2 observations at 19.35 GHz agree well with our modeled

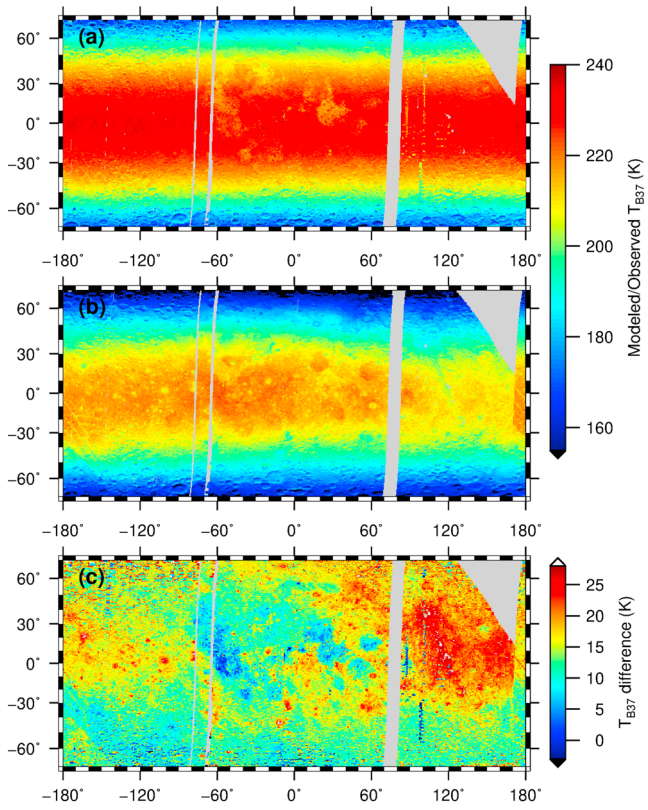

Figure 8. Comparison of T_{B37} near midnight. (a) Model calculated T_{B37}. (b) CE-2 T_{B37} observations. (c) T_{B37} differences between model calculated and CE-2 observations near midnight within 70° N/S latitudes. The gray gaps denote the lack of coverage of CE-2 Microwave RadioMeter data within the time range 23:00–01:00.

values. This indicates that these two data sets recorded a similar surface/subsurface thermal environment near midnight with similar data quality. However, there is a large difference between CE-1 and CE-2 observations when compared to our simulation results at 37 GHz (Figure 6b). This could indicate that the lunar surface thermal environment observed by CE-1 and CE-2 at the same local time and the same 37-GHz channel exhibited different behavior. However, it is more likely that the difference between the CE-1 and CE-2 observations is caused by calibration uncertainties in the CE-2 37-GHz channel data. The uncertainties in T_{B37} are likely larger than those at T_{B19} because of lunar surface heat contaminations (Hu et al., 2017) because the 37-GHz channel is more sensitive to surface temperatures. The better agreement of CE-1 observations with our simulation results suggests that CE-1 T_{B37} data are of better data quality than that of CE-2.

Considering the discrepancies and analysis from our comparison, we propose to quantify the biases in order to modify and improve the CE-2 MRM data. As shown in Figures 7a and 8a, we modeled TT_{B19} and T_{B37} at the same local times as the CE-2 observations (Figures 7b and 8b) at each cell in the low to middle latitudes. The gray gaps denote the lack of coverage of CE-2 data in the time range of 23:00–01:00. As expected, the model calculated T_{B19} presents a similar distribution as the CE-2 observations, although the observed T_{B37} is much lower than that of our simulation results. Note that both T_{B19} and T_{B37} maps measured by CE-2 are dotted by some "cold" areas which are not shown in our simulated T_B maps. These thermal anomalies are likely caused by regolith inhomogeneities, which are not taken into account in our thermal model.

In order to assess the differences between the observations and simulation results, we computed T_B difference maps which show the modeled T_B minus the observed T_B at each cell, that is, $\Delta T_{Bi} = T^s_{Bi} - T^o_{Bi} (i = 19, 37)$, where "s" and "o" denote the simulation and observation, respectively. As shown in Figures 7c and 8c, both ΔT_{B19} and ΔT_{B37} maps present different biases at low to middle latitudes of the Moon. The values of ΔT_{B19} are mainly limited to the range −5 to +5 K, whereas for ΔT_{B37}, the differences fall mainly between 0 and +25 K. To evaluate the biases of each map, we also present the data density for comparison between

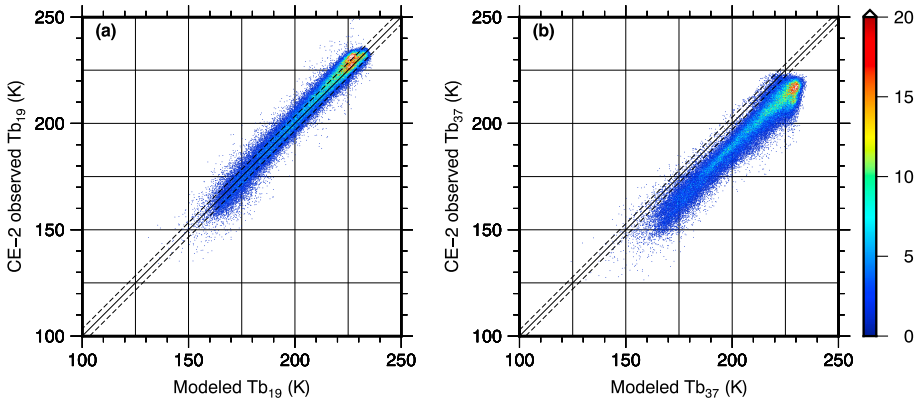

Figure 9. Scatter plots between CE-2 observations and modeled T_B at (a) 19.35 and (b) 37 GHz near midnight within 70° N/S latitudes. The point clouds are color-coded to show the density of points (see scale on the right side). The black solid lines are the 1:1 line, and the dashed lines are one standard deviation of each data cluster above and below the solid lines.

the modeled and observed T_B (Figure 9). The standard deviations for ΔT_{B19} and ΔT_{B37} are 3.40 and 2.88 K, respectively. Thus, as shown in Figure 9, about 63.18% of the total points between 70° N and 70° S have $|T_{B19}| < 3.40$ K. But for ΔT_{B37}, only ~0.01% of the total points in the same latitude range have $|T_{B37}| < 2.88$ K, indicating the much larger offset between the modeled and observed T_B at 37 GHz. This suggests that the T_{B19} values obtained by CE-2 MRM are more accurate, while there are greater calibration uncertainties in T_{B37}.

5.2. Modification of CE-2 MRM Data

Comparison of T_B between CE-1/2 observations and our simulation results shows that CE-2 MRM data present larger departures than that of CE-1, especially in the 37-GHz channel. The discrepancies might be caused by the method of in-orbit calibration or perhaps by the different sizes of the field of view. For the CE-2 observations, however, both the 19.35- and 37-GHz channels worked under the same conditions and used the same calibration method, yet there exists a larger departure from the model results in the 37-GHz data than in 19.35 GHz. Here we note that the lower altitude of the CE-2 orbit (half of CE-1's) allowed a larger area of the warm lunar surface to intrude into the field of view of the cold-reference antennas at certain times during in-orbit calibration (Hu et al., 2017; Siegler & Feng, 2017). In addition, due to the relatively short wavelength of the 37-GHz channel, it is more sensitive to surface temperature compared to 19.35 GHz (Hu et al., 2017). As a result, greater error from this surface heat contamination might be present in the calibrated CE-2 MRM data, especially for the 37-GHz data.

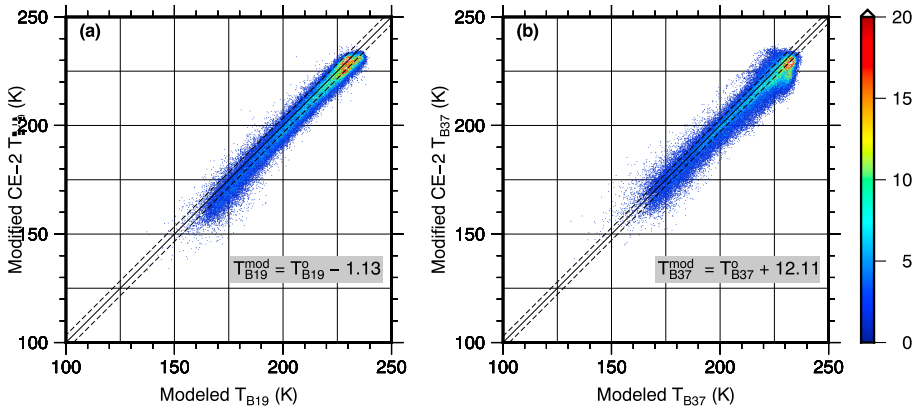

Figure 10. Scatter plots between modified CE-2 observations and simulation results at (a) 19.35 and (b) 37 GHz near midnight within 70° N/S latitudes. The point clouds are color-coded to show to density of points (see scale on the right side). The black solid lines are the 1:1 line, and the dashed lines are one standard deviation of each data cluster above and below the solid lines.

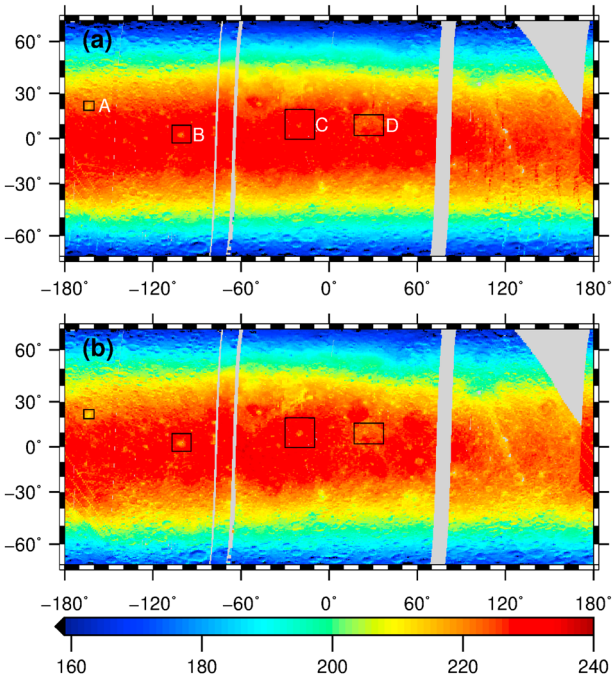

Figure 11. Maps of the modified CE-2 Microwave RadioMeter data at (a) 19.35 and (b) 37 GHz near midnight at low to middle latitudes of the Moon. The boxes A–D denote the microwave low-T_B regions. A = Jackson crater; B = Pierazzo crater; C = Copernicus crater; D = northern Mare Tranquillitatis.

Although the simulated T_B from our improved thermal model cannot completely eliminate uncertainties related to topographic effects or internal heat flow, we contend that our simulations are validated by their consistency with CE-1 observations. Future lunar mission or ground-based observations at the MRM frequencies could provide more data for comparing with CE-1/2 observations and further verifying our simulation results. Here we assume that the uncertainties in the CE-2 observations were caused by thermal contamination of the cold-reference antennas (Hu et al., 2017; Siegler & Feng, 2017) and propose a simple empirical normalization to modify the midnight data. We apply an approach following the work of Hu et al. (2017) to modify the CE-2 observations:

$$T_{Bi}^{modified} = T_{Bi}^{o} + \langle \Delta T_{Bi} \rangle \quad (i = 19, 37), \tag{7}$$

where $T_B^{modified}$ is the modified value of T_B, and $\langle \Delta T_B \rangle$ is the averaged biases between simulation results and CE-2 MRM observations.

Figure 10 shows the cross plot of data density between the modified (normalized) T_B and the modeled T_B. Both $T_{B19}^{modified}$ and $T_{B37}^{modified}$ correlate well with T_{B19}^{s} and T_{B37}^{s}. Comparing to the standard deviation, the total numbers of $|T_{B19}^{s} - T_{B19}^{modified}| < 3.40$ K and $|T_{B37}^{s} - T_{B37}^{modified}| < 2.88$ K are ~80.20% and ~66.85%, respectively. It suggests that the modification has improved the accuracy of T_{B19} and T_{B37} data. The biases of $\langle \Delta T_B \rangle$ are +12.11 and −1.13 K at 37 and 19.35 GHz, respectively. Statistically, it suggests that the 37-GHz channel is influenced by 12.11 K of heat contamination, while only −1.13 K uncertainty caused by heat contamination in 19.35 GHz. Here the sign of $\langle \Delta T_B \rangle$ (positive for 37 GHz and negative for 19.35 GHz) just results from the differences between simulations and observations, and it does not have a de facto physical meaning. The larger bias in T_{B37} strongly suggests greater heat contamination of 37-GHz channel than that of the 19.35-GHz channel during the in-orbit data calibration. It is worth noting that the variations in rock concentration and inhomogeneity of the regolith are neglected in our thermal model. Further work considering these factors could improve the simulation accuracy and modification of T_B. Nevertheless, caution should be used when interpreting the absolute values of CE-2 MRM high-frequency T_B data before evaluation and empirical adjustment are conducted.

5.3. Examination of Features With Low Midnight T_B

Figure 11 shows the maps of $T_{B19}^{modified}$ and $T_{B37}^{modified}$. Comparing to T_B maps shown in Figures 7b and 8b, the modified T_B data can reveal more accurately the thermal regime of the lunar subsurface. Several

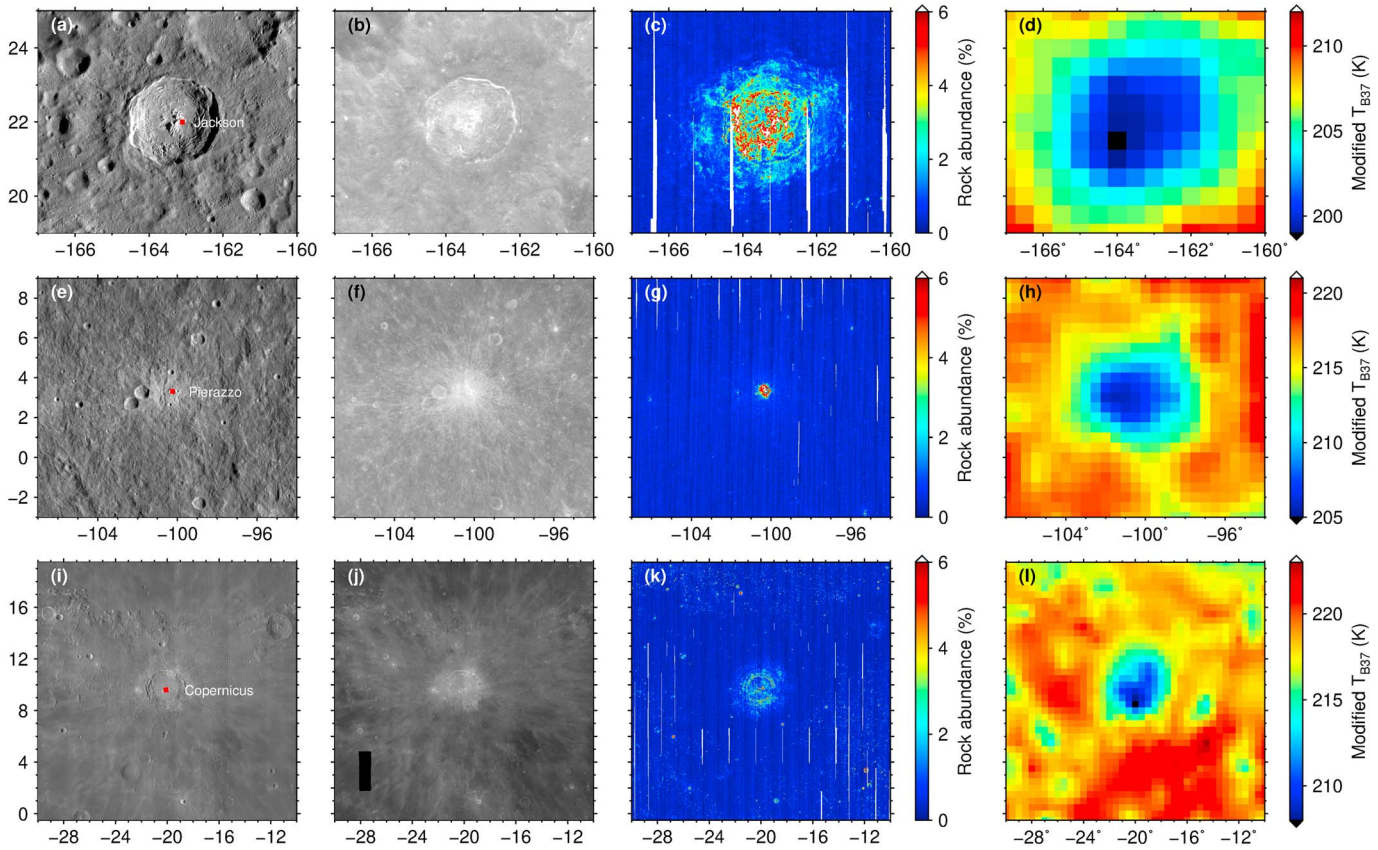

Figure 12. Comparison of microwave low-T_B regions at craters of Jackson (top row, corresponding to box A of Figure 11), Pierazzo (middle row, corresponding to box B of Figure 11), and Copernicus (bottom row, corresponding to box C of Figure 11). (a), (e), and (i) are morphology images obtained by Lunar Reconnaissance Orbiter Camera Wide Angle Camera. (b), (f), and (j) are Clementine 750-nm images obtained at relatively small phase angles, emphasizing differences in albedo. (c), (g), and (k) are Diviner rock abundance distribution maps (Bandfield et al., 2011), obtained from the Planetary Data System. (d), (h), and (l) are distributions of modified T_{B37} from Figure 11b with new color codings.

low-T_B (relatively cold) regions have been identified on the modified midnight T_B maps (boxes A–D in Figure 11). Recent studies of CE-2 level 2C MRM data (Zheng et al., 2019; Zhu et al., 2019) have also reported these anomalies. Strictly speaking, the observations with greater accuracy can reveal more information about the nature of geological features. For example, the empirically normalized T_B data could lead to better understanding of the regolith thermal properties, thickness, and subsurface thermal regime of the Moon especially at these low-T_B regions. Considering the factors (surface albedo, rock abundance, and ilmenite content) that have the greatest influence on microwave observations, we found that these low-T_B regions are characterized by two types of geological features.

(1) Regions A–C (Figure 12). These areas correspond to impact craters (cf. Zheng et al., 2019) and have also been identified as having a high abundance of rocks (Bandfield et al., 2011), small H-parameter, or high thermal inertial (Hayne et al., 2017). The low midnight T_B at 19.35 and 37 GHz associated with these features can be attributed to high rock abundance. A greater abundance of rock fragments leads to a higher loss tangent than fine-grained soil lacking rocks, which in turn tends to suppress microwave emissions at night and thus results in lower observed T_B (Zheng et al., 2019).

For example, consider the 9-km-diameter crater Pierazzo (Figure 12e). The crater has obvious high surface albedo (Figure 12f) and is a microwave low-T_B spot (Figure 12h), though its diameter (Figures 12d and 12f) is much smaller than that of Jackson and Copernicus craters (Figures 12a, 12i, 12b, and 12j). The high rock abundance associated with the interiors and near-rim ejecta of these craters (Figures 12c, 12g, and 12k) cause cold regions in MRM midnight observations (Figures 12d, 12h, and 12l). For Pierazzo, rocky impact melt flows are found at distances of up to 40 km from the crater (Braya et al., 2018). However, in contrast with the Diviner thermal-infrared measurements, the longer wavelengths of MRM observations yield information

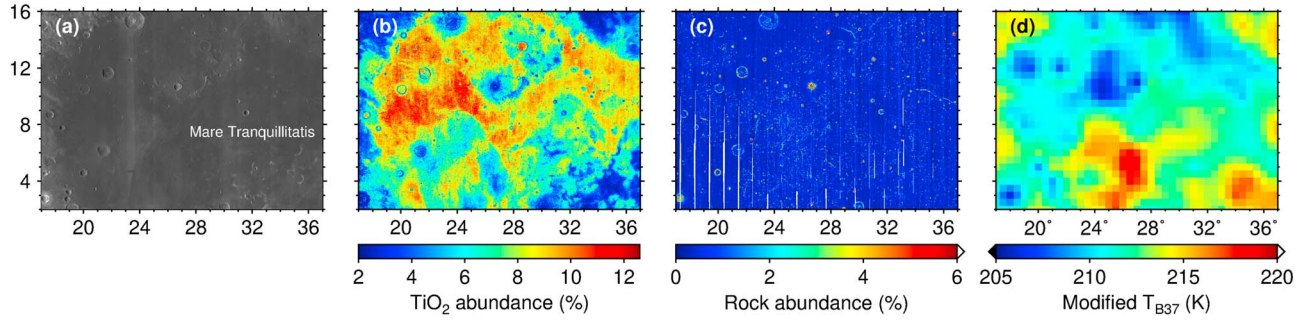

Figure 13. Shown is microwave low-T_B region D of Figure 11 corresponding to (a) Lunar Reconnaissance Orbiter Camera Wide Angle Camera image, (b) TiO_2 abundance, and (c) rock abundance distribution (Bandfield et al., 2011), and (d) distribution of modified T_{B37} from Figure 11b with new color coding. Here we show the TiO_2 distribution of Sato et al. (2017) because of its greater accuracy for lunar mare regions.

about the properties of the subsurface, suggesting that the high rock abundance of these craters persists from the surface to the penetration depth of 19.35- and 37-GHz microwaves (tens of centimeters in highland regolith).

(2) Region D (Figure 13). This low microwave T_B region in northern Mare Tranquillitatis (Figure 13a) has been reported as exhibiting a day/night T_B anticorrelation (Chan et al., 2010; Zheng et al., 2019). It reaches much higher T_B than the surroundings in the day time but has lower T_B at night. Similar thermal behavior has also been found in northern Oceanus Procellarum (Chan et al., 2010; Zheng et al., 2019, 2012). Unlike the regions A–C, northern Mare Tranquillitatis has quite low albedo and lesser rock abundance (Figure 13c) but the highest TiO_2 values (Figure 13b) on the Moon (Sato et al., 2017). As discussed by Zheng et al. (2019), the high content of the Ti-bearing mineral ilmenite ($FeTiO_3$) in Tranquillitatis basalts causes a high microwave loss tangent, making the regolith more opaque to microwave emissions. Thus, in areas with a high abundance of TiO_2, microwave emission at night originates closer to the surface (which has cooled relatively quickly) resulting in lower observed nighttime T_B (Figure 13d).

Therefore, the low nighttime T_B of regions such as Mare Tranquillitatis is also related to the presence of material enriched in ilmenite. Further investigation of the influence of ilmenite content on microwave properties could lead to new techniques for mapping TiO_2 abundance (Zheng et al., 2012).

5.4. Future Applications of the Model

Combined with Diviner data, the empirically modified CE-2 T_B data in our study could provide more accurate information on the nighttime subsurface thermal regime. This in turn determines the accuracy of inversion results for quantities such as regolith thickness, subsurface temperature, and heat flow. For example, one of CE-1/2's scientific goals was to investigate the global regolith thickness. Application of our improved thermal model could provide a means for higher-fidelity mapping of regolith thickness, thus aiding in our understanding of the evolution of the lunar regolith. In addition, He-3 implanted from the solar wind may be an important energy source for future human missions and lunar base construction (see Fa & Jin, 2007a, and references therein). However, previous models for estimating the He-3 abundance in the regolith have neglected the effects on inverting regolith thickness related to topography, inhomogeneous surface emissivity, and the calibration uncertainties of the CE-2 MRM data. Employing our improved thermal model and modified CE-2 MRM data will permit more accurate estimation of the regolith thickness and He-3 abundance.

As mentioned above, the dielectric constant of the regolith is a key parameter controlling microwave emission. The dielectric properties of regolith are mainly dependent upon the bulk density and the ilmenite content (Carrier et al., 1991; Fa & Jin, 2007b). Bulk density is controlled by the overturn history at a particular location, while ilmenite content is a function of the chemical composition and petrologic history of the material. Our improved thermal model could form the basis of an inversion for dielectric constant, which could also employ the empirically adjusted CE-2 MRM data. The retrieved dielectric constants corresponding to the different penetration depths of MRM frequencies could provide us with a better understanding of the impact and volcanic stratigraphy of the lunar surface.

In order to properly carry out normalization to modify the CE-2 MRM daytime data to account for the contamination of the cold-reference antennas, it is necessary to model T_B accurately. Further work such as

using a 3-D thermal model could improve the retrieved subsurface temperature and T_B simulations. Additionally, to investigate the microwave low T_B regions that have been identified in CE-2 observations, Diviner H-parameter (Hayne et al., 2017) and rock abundance (Bandfield et al., 2011) could, for example, be taken into account to extend our thermal model. Based on these methods, it would be possible to modify the CE-2 MRM diurnal data in future work.

6. Conclusions

In this study, we employed the surface bolometric brightness temperatures (T_{Bol}) derived from Diviner thermal-infrared data as a constraint on the surface temperature. The diurnal variation of T_{Bol} inherently includes the effects of topographic relief, rock abundance, surface albedo, surface roughness, and infrared emissivity. Using our improved thermal model, we calculated the average diurnal temperatures at a depth of 1 m as an example. We find that the physical temperatures are significantly influenced by both latitude and surface topography. By representing the lunar regolith as a half-space that is inhomogeneous with depth, we then simulated the microwave brightness temperature at 19.35 and 37 GHz (0.81- and 1.55-cm wavelength, respectively) near lunar midnight based on our improved thermal model. We found that at high latitudes, brightness temperature is mainly controlled by topographic relief. For mare regions, T_{B19} is higher than that of T_{B37} due to the larger penetration depth of 19.35-GHz radiation. Some geologic features such as Mare Orientale and Mare Moscoviense stand out in the modeled T_{B19} map; these anomalies may be related to contrasts with the surroundings in terms of physical characteristics such as the abundance of fragments and regolith compactness. In addition, certain thermal anomalies in our model T_{B37} map, such as Mare Tranquillitatis and parts of Oceanus Procellarum, exhibit midnight brightness temperatures that are lower than that of their surroundings, likely due to increased ilmenite content (Zheng et al., 2019, 2012). However, some low-T_B spots found in maps of CE-1/2 observed MRM T_B do not appear in maps derived from our thermal model. These features are associated with young impact craters, and the difference between the model and observation may be caused by variations in surface/subsurface rock abundances that are not considered in our model.

Comparing the CE-1/2 observations to our simulated T_B at the same local time and latitudes, we found that CE-1 observations are likely of better data quality than those of CE-2's, especially for the 37-GHz channel. That is, the T_{B37} data obtained by CE-2 MRM clearly have larger uncertainties in calibration than T_{B19}. Since 37-GHz emissions are more sensitive to surface temperature, the problem is likely related to greater heat contamination from the lunar surface affecting the CE-2 cold-reference antenna (Hu et al., 2017). Based on this assumption, we empirically normalized (modified) the CE-2 MRM data near midnight following the approach of Hu et al. (2017). The results suggest that the accuracy of the modified T_B data sets has been improved substantially. For example, the total numbers of $|T^s_{B19} - T^{modified}_{B19}| < 3.40$ K (standard deviation) and $|T^s_{B37} - T^{modified}_{B37}| < 2.88$ K (standard deviation) are ~80.20% and ~66.85%, respectively. The high accuracy of the simulation results produced by our method is promising for future work with MRM data involving the inversion of dielectric properties, thickness of regolith, and evaluation of He-3 abundance.

Low-T_B regions form a prominent class of anomalies in the modified microwave brightness temperature maps; these areas have notably lower T_B than the surroundings. Examining the geological features that are present at these locations, we found that the low-T_B regions correspond to two types: (1) low-T_B at fresh craters with a high abundance of rock fragments and bright rays (boxes A–C in Figure 11) and (2) high-Ti mare surfaces with low Diviner rock abundance (box D in Figure 11). Examples of this type, such as northern Mare Tranquillitatis, are revealed by T_B data due to the high microwave loss tangent of the high-Ti basalts and corresponding suppression of microwave emissions from depth.

These two types of low-T_B regions are caused by different mechanisms that relate to the different geological settings. Because of the large penetration depth of microwaves relative to optical and thermal-infrared wavelengths, MRM sensing can provide information on the nature of the subsurface and thus improve our understanding of the evolution of regolith on the Moon.

Acknowledgments
The paper greatly benefitted from thoughtful reviews by Joshua Bandfield and Matthew Siegler. G. W. was supported by opening fund of State Key Laboratory of Lunar and Planetary Sciences (Macau University of Science and Technology; Macau FDCT grant 119/2017/A3), West Light Foundation of the Chinese Academy of Sciences, National Natural Science Foundation of China (41803052) and was also supported from China Scholarship Council. X. L. was supported by the National Natural Science Foundation of China (41572037; Major Program: 41490630) and Youth Innovation Promotion Association of CAS (2014359). D. T. B. acknowledges support from NASA Lunar Data Analysis Program grant NNX16AN55G. The Diviner T_{Bol} data set was obtained from the NASA Planetary Data System Geosciences Node, available at http://pds-geosciences.wustl.edu/missions/lro/diviner.htm. CE-1/2 microwave radiometer data were provided by the Ground Research and Application System of Chinese Lunar Exploration Program and are available online (http://moon.bao.ac.cn). Figures were created using the Generic Mapping Tools of Wessel and Smith (1991).

References

Bandfield, J. L., Ghent, R. R., Vasavada, A. R., Paige, D. A., Lawrence, S. J., & Robinson, M. S. (2011). Lunar surface rock abundance and regolith fines temperatures derived from LRO Diviner Radiometer data. *Journal of Geophysical Research*, *116*, E00H02. https://doi.org/10.1029/2011JE003866

Bandfield, J. L., Hayne, P. O., Williams, J. P., Greenhagen, B. T., & Paige, D. A. (2015). Lunar surface roughness derived from LRO Diviner Radiometer observations. *Icarus*, *248*, 357–372.

Blewett, D., Zheng, Y. C., Chan, K., Hu, G., Neish, C., Tsang, K., & Zhu, Y. (2018). Chang'E-2 microwave brightness temperature maps of the Moon. In *Lunar and Planetary Science Conference* (Vol. 49).

Braya, V. J., Atwood-Stonea, C., Neish, C. D., Artemievad, N. A., McEwena, A. S., & McElwained, J. N. (2018). Lobate impact melt flows within the extended ejecta blanket of Pierazzo crater. *Icarus*, *301*, 26–36.

Carrier, W., Mitchell, J., & Mahmood, A. (1973). The relative density of lunar soil. In *Proceedings of the Lunar Science Conference* (Vol. 4, pp. 2403–2411). Houston.

Carrier, W., Olhoeft, G., & Mendell, W. (1991). Physical properties of the lunar surface. In G. H. Heiken, D. T. Vaniman, & B. M. French (Eds.), *Lunar Sourcebook: A User's Guide to the Moon* (pp. pp 475–594). New York: Cambridge University Press.

Chan, K. L., Tsang, K. T., Kong, B., & Zheng, Y. C. (2010). Lunar regolith thermal behavior revealed by Chang'E-1 microwave brightness temperature data. *Earth and Planetary Science Letters*, *295*(1), 287–291. https://doi.org/10.1016/j.epsl.2010.04.015

Crank, J., & Nicolson, P. (1947). A practical method for numerical evaluation of solutions of partial differential equations of the heat-conduction type. *Mathematical Proceedings of the Cambridge Philosophical Society*, *43*(1), 50–67. https://doi.org/10.1017/S0305004100023197

Fa, W., & Jin, Y. (2007a). Quantitative estimation of helium-3 spatial distribution in the lunar regolith layer. *Icarus*, *190*(1), 15–23. https://doi.org/10.1016/j.icarus.2007.03.014

Fa, W., & Jin, Y. Q. (2007b). Simulation of brightness temperature from lunar surface and inversion of regolith-layer thickness. *Journal of Geophysical Research*, *112*, E05003. https://doi.org/10.1029/2006JE002751

Fa, W., & Jin, Y. (2010). Analysis of microwave brightness temperature of lunar surface and inversion of regolith layer thickness: Primary results of Chang'E-1 multi-channel radiometer observation. *Science China*, *53*(1), 168–181.

Fa, W., & Wieczorek, M. A. (2012). Regolith thickness over the lunar nearside: Results from Earth-based 70-cm Arecibo radar observations. *Icarus*, *218*(2), 771–787. https://doi.org/10.1016/j.icarus.2012.01.010

Fang, T., & Fa, W. (2014). High frequency thermal emission from the lunar surface and near surface temperature of the Moon from Chang'E-2 microwave radiometer. *Icarus*, *232*, 34–53.

Feng, J., Zou, Y., Bian, W., Zheng, Y., & Li, C. (2010). Review on physical models of lunar brightness temperature. *Chinese Journal of Geochemistry*, *29*(2), 204–211. https://doi.org/10.1007/s11631-010-0204-9

Gary, B. L., & Keihm, S. J. (1978). Interpretation of ground-based microwave measurements of the Moon using a detailed regolith properties model. In *Lunar and Planetary Science Conference Proceedings* (Vol. 9, pp. 2885–2900).

Gillis, J. J., Jolliff, B. L., & Elphic, R. C. (2003). A revised algorithm for calculating TiO_2 from Clementine UVVIS data: A synthesis of rock, soil, and remotely sensed TiO_2 concentrations. *Journal of Geophysical Research*, *108*(E2), 5009. https://doi.org/10.1029/2001JE001515

Gong, X., & Jin, Y. (2012). Diurnal physical temperature at Sinus Iridum area retrieved from observations of Chinese Chang'E-1 microwave radiometer. *Icarus*, *218*(2), 807–816.

Gong, X., Paige, D., Siegler, M., & Jin, Y. (2015). Inversion of dielectric properties of the lunar regolith media with temperature profiles using change microwave radiometer observations. *IEEE Geoscience and Remote Sensing Letters*, *12*(2), 384–388.

Hayne, P. O., Bandfield, J. L., Siegler, M. A., Vasavada, A. R., Ghent, R. R., Williams, J. P., et al. (2017). Global regolith thermophysical properties of the Moon from the Diviner Lunar Radiometer Experiment. *Journal of Geophysical Research: Planets*, *122*, 2371–2400. https://doi.org/10.1002/2017JE005387

Hayne, P. O., Greenhagen, B. T., Foote, M. C., Siegler, M. A., Vasavada, A. R., & Paige, D. A. (2010). Diviner Lunar Radiometer observations of the LCROSS impact. *Science*, *330*(6003), 477–479.

Hu, G. P., Chan, K. L., Zheng, Y. C., Tsang, K. T., & Xu, A. A. (2017). Comparison and evaluation of the Chang'E microwave radiometer data based on theoretical computation of brightness temperatures at the Apollo 15 and 17 sites. *Icarus*, *294*, 72–80. https://doi.org/10.1016/j.icarus.2017.04.009

Hu, G. P., Zheng, Y. C., & Xu, A. A. (2016). Microwave brightness temperature of the moon: The possibility of setting a calibration source of the lunar surface. *IEEE Geoscience and Remote Sensing Letters*, *13*(2), 182–186.

Huang, S. (2008). Surface temperatures at the nearside of the Moon as a record of the radiation budget of Earths climate system. *Advances in Space Research*, *41*(11), 1853–1860.

Jones, W. P., Watkins, J. R., & Calvert, T. A. (1975). Temperatures and thermophysical properties of the lunar outermost layer. *The Moon*, *13*(4), 475–494.

Keihm, S. (1984). Interpretation of the lunar microwave brightness temperature spectrum: Feasibility of orbital heat flow mapping. *Icarus*, *60*, 568–589.

Keihm, S., & Cutts, J. (1981). Vertical-structure effects on planetary microwave brightness temperature measurements: Applications to the lunar regolith. *Icarus*, *48*(2), 201–229.

Keihm, S., & Langseth, M. (1973). Surface brightness temperatures at the Apollo 17 heat flow site: Thermal conductivity of the upper 15 cm of regolith. In *Proceedings of the Lunar Science Conference* (Vol. 4, pp. 2503–2513). Houston.

Langseth, M. G., Keihm, S. J., & Peters, K. (1976). Revised lunar heat-flow values. In *Lunar and Planetary Science Conference Proceedings* (Vol. 7, pp. 3143–3171). Houston.

Ledlow, M. J., Zeilik, M., Burns, J. O., Gisler, R., Zhao, J. H., & Baker, D. N. (1992). Subsurface emissions from Mercury-VLA radio observations at 2 and 6 centimeters. *The Astrophysical Journal*, *384*, 640–655.

Linsky, J. L. (1966). Models of the lunar surface including temperature-dependent thermal properties. *Icarus*, *5*(1-6), 606–634.

Meng, Z., Chen, S., Osei, E. M., Wang, Z., & Cui, T. (2010). Research on water ice content in Cabeus crater using the data from the microwave radiometer onboard Chang'E-1 satellite. *Science China Physics, Mechanics and Astronomy*, *53*(12), 2172–2178. https://doi.org/10.1007/s11433-010-4159-y

Meng, Z., Xu, Y., Cai, Z., Chen, S., Lian, Y., & Huang, H. (2014). Influence of lunar topography on simulated surface temperature. *Advances in Space Research*, *54*(10), 2131–2139.

Montopoli, M., Carlofelice, A. D., Tognolatti, P., & Marzano, F. S. (2011). Remote sensing of the Moon's subsurface with multifrequency microwave radiometers: A numerical study. *Radio Science*, *46*, RS1012. https://doi.org/10.1029/2009RS004311

Pabari, J. (2016). Dependence of lunar Mare microwave brightness temperature on FeO and TiO_2. *Planetary and Space Science*, *132*, 1–12. https://doi.org/10.1016/j.pss.2016.08.008

Paige, D. A., Foote, M., Greenhagen, B., Schofield, J., Calcutt, S., Vasavada, A., et al. (2010). The Lunar Reconnaissance Orbiter Diviner Lunar Radiometer Experiment. *Space Science Reviews*, *150*(1-4), 125–160.

Paige, D. A., Siegler, M. A., & Zhang, J. A. (2010). Diviner Lunar Radiometer Observations of cold traps in the Moon's south polar region. *Science*, *330*, 479–482.

Pettit, E., & Nicholson, S. B. (1930). Lunar radiation and temperatures. *Astrophysical Journal*, *71*(71), 102–135.
Sandor, B. (1995). Microwave observation and modeling of a lunar eclipse. *Icarus*, *115*(2), 387–398.
Sato, H., Robinson, M. S., Lawrence, S. J., Denevi, B. W., Hapke, B., Jolliff, B. L., & Hiesinger, H. (2017). Lunar mare TiO_2 abundances estimated from UV/Vis reflectance. *Icarus*, *296*, 216–238.
Shkuratov, Y. G., & Bondarenko, N. V. (2001). Regolith layer thickness mapping of the Moon by radar and optical data. *Icarus*, *149*(2), 329–338.
Siegler, M. A., & Feng, J. (2017). Microwave remote sensing of lunar subsurface temperatures: Reconciling Chang'E MRM and LRO Diviner. In *Lunar and Planetary Science Conference Abstract 1705* (Vol. 48). *Woodlands*.
Siegler, M. A., Paige, D. A., Williams, J. P., & Bills, B. (2015). Evolution of lunar polar ice stability. *Icarus*, *255*, 78–87.
Vasavada, A. R., Bandfield, J. L., Greenhagen, B. T., Hayne, P. O., Siegler, M. A., Williams, J. P., & Paige, D. A. (2012). Lunar equatorial surface temperatures and regolith properties from the Diviner Lunar Radiometer Experiment. *Journal of Geophysical Research*, *117*, E00H18. https://doi.org/10.1029/2011JE003987
Vasavada, A. R., Paige, D. A., & Wood, S. E. (1999). Near-surface temperatures on Mercury and the Moon and the stability of polar ice deposits. *Icarus*, *141*, 179–193.
Wang, Z., Li, Y., Jiang, J., & Li, D. (2010). Lunar surface dielectric constant, regolith thickness, and ^{3}He abundance distributions retrieved from the microwave brightness temperatures of CE-1 Lunar Microwave Sounder. *Science China Earth Sciences*, *53*(9), 1365–1378. https://doi.org/10.1007/s11430-010-4022-z
Wang, Z., Li, Y., Zhang, X., Jiang, J., Xu, C., Zhang, D., & Zhang, W. (2010). Calibration and brightness temperature algorithm of CE-1 Lunar Microwave Sounder (CELMS). *Science China Earth Sciences*, *53*(9), 1392–1406. https://doi.org/10.1007/s11430-010-4008-x
Wang, Z., Li, Y., Zhang, D., Jiang, J., Zhao, J., Hua, F., & Zhang, X. (2010). Prelaunch calibration of Chang'E-2 Lunar Microwave radiometer. In *2010 International Conference on Microwave and Millimeter Wave Technology* (pp. 1551–1554). Chengdu.
Wei, G., Li, X., & Wang, S. (2016a). Inversions of subsurface temperature and thermal diffusivity on the Moon based on high frequency of Chang'E-1 microwave radiometer data. *Icarus*, *275*, 97–106. https://doi.org/10.1016/j.icarus.2016.04.014
Wei, G., Li, X., & Wang, S. (2016b). Thermal behavior of regolith at cold traps on the Moon's south pole: Revealed by Chang'E-2 microwave radiometer data. *Planetary and Space Science*, *122*, 101–109.
Wessel, P., & Smith, W. H. (1991). Free software helps map and display data. *Eos Transactions American Geophysical Union*, *72*(41), 441–446.
Williams, J. P., Paige, D. A., Greenhagen, B. T., & Sefton-Nash, E. (2017). The global surface temperatures of the Moon as measured by the Diviner Lunar Radiometer Experiment. *Icarus*, *283*, 300–325.
Zheng, Y., Chan, K. L., Tsang, K. T., Zhu, Y. C., Hu, G. P., Blewett, D. T., & Neish, C. (2019). Analysis of Chang'E-2 brightness temperature data and production of high spatial resolution microwave maps of the Moon. *Icarus*, *319*, 627–644.
Zheng, Y., Tsang, K., Chan, K., Zou, Y., Zhang, F., & Ouyang, Z. (2012). First microwave map of the Moon with Change-1 data: The role of local time in global imaging. *Icarus*, *219*(1), 194–210. https://doi.org/10.1016/j.icarus.2012.02.017
Zhou, M., Zhou, J., Zhang, X., & Wang, F. (2010). Inversion of microwave brightness temperature data for estimating lunar regolith thickness. *International Journal of Applied Electromagnetics and Mechanics*, *33*(3-4), 1041–1048. https://doi.org/10.3233/JAE-2010-1218
Zhu, Y., Zheng, Y., Fang, S., Zou, Y., & Pearson, S. (2019). Analysis of the brightness temperature features of the lunar surface using 37 GHz channel data from the Chang'E-2 microwave radiometer. *Advances in Space Research*, *63*(1), 750–765.